WILEY-VCH

Stressmechanically Reconfigurable Chiroptical Meta-devices in Visible Band

Lu Zhang, Jie Wang, Lei Xu, Feng Gao, Wending Zhang, and Ting Mei**

L. Zhang, Prof. W. Zhang, Prof. T. Mei
Key Laboratory of Light Field Manipulation and Information Acquisition, Ministry of Industry and Information Technology, School of Physical Science and Technology, Northwestern Polytechnical University, Xi'an 710129, China
E-mail: zhangwd@nwpu.edu.cn; ting.mei@ieee.org
Prof. J. Wang
Analytical & Testing Center, Northwestern Polytechnical University, Xi'an 710129, China
Prof. L. Xu
Advanced Optics & Photonics Laboratory, Nottingham Trent University, Nottingham NG11 8NS, United Kingdom
Prof. F. Gao
MOE Key Laboratory of Weak-Light Nonlinear Photonics, TEDA Applied Physics Institute and School of Physics, Nankai University, Tianjin 300457, China

Keywords: reconfigurable chiroptical meta-device, chiral plasmonic, active regulation, flexible device, circular dichroism

Abstract: The development of low-cost and convenient procedure to produce large-area reconfigurable chiroptical meta-devices (CMDs) enantiomers with dynamically tunable chiroptical response in the visible band has generated significant interest, owing to its tremendous potential for applications such as optical rotary filtering, color switching, information storage, etc. Currently, many methods, such as phase change material, air pressure, bias, etc., have been proposed to reconfigure the chiroptical response of the CMDs enantiomers, but still lack of ability to actively regulate the chiroptical response of the large-area CMDs. Herein, we propose the centimeter-scale stressmechanically reconfigurable CMDs enantiomers with actively-tunable chiroptical response in the visible band. The chirality sign switching and chirality intensity turning on-off of the CMDs enantiomers can be achieved by bending the flexible substrate to the desired curvature radius to turn the electromagnetic modes resonance of the CMDs enantiomers. Our results provide an effective approach to supply the large-area

reconfigurable CMDs enantiomers with actively tunable chiroptical response, and will open up new possibilities for chirality nanophotonic applications.

1. Introduction

Chiral molecules, with a feature of structurally symmetric but not completely coincident, exhibit distinct optical responses when interacting with circularly polarized light. Benefiting from the understanding of natural chiral molecules, artificially designed chiroptical meta-devices (CMDs) enantiomers can exhibit remarkably strong chiroptical response, and play an important role to probe the chirality at the nanoscale by enhancing chiral light-matter interactions, holding promise for chiral-optical applications, including chiral biomolecular sensing,[1] chiral enantiomer differentiation,[2] circularly polarized light detection,[3] chiral mirror,[4] broadband circular polarizer,[5] etc.

Currently, the CMDs enantiomers constructed by metal or dielectric materials lack active tunability, which restricts their potential applications across various fields. To address this issue, various methods have been proposed to regulate the chiroptical response of the CMDs enantiomers. Phase change materials have been employed to reconfigure the resonant behaviors of the electromagnetic modes in the CMDs. This is achieved by leveraging the substantial alterations in dielectric coefficients of phase change materials when transition from an amorphous to a crystalline state.[6] The near-field coupling characteristic of the CMDs was reconfigured by utilizing the swelling properties of the silk fibroin films.[7] Based on the redox reaction of PbO_2 under ultraviolet light irradiation, the longitudinal and transverse modes of the gold nanorods-based CMDs can be reconfigured.[8] To date, the electromagnetic response of the CMDs has been successfully reconfigured using various external stimuli such as macroscopic stacking,[9] thermal,[10] light intensity,[11] air pressure,[12] PH[13] and bias.[14] These techniques have been widely used in fields such as rotary filtering,[15] information storage[16] and color switching,[17] etc. Nevertheless, there is still a lack of effective strategies to actively manipulate the chiroptical response of the large-area CMDs enantiomers in the visible band.

In this work, we present a novel approach to prepare the flexible CMDs enantiomers with a stressmechanically reconfigurable chiroptical response in the visible band. By stressmechanical-bending the flexible substrate to manipulate the resonance characteristics of the electromagnetic modes in the CMDs, we have achieved chirality sign switching and chirality intensity turning on-off. The circular dichroism (CD) examination result has shown that the chirality sign of the CMDs can be switched at the wavelength of 441 nm, with the CD intensity modulation from 230 mdeg to -210 mdeg. At the wavelength of 654 nm, the chirality

intensity of the CMDs can be turn on-off, with the CD intensity modulation from 900 mdeg to 30 mdeg. Most importantly, the chiroptical response of the stressmechanically reconfigurable CMDs enantiomers exhibits continuous tunability, allowing it to be precisely adjusted to the desired state by controlling the bending radius of the flexible CMDs.

2. Results and Discussion

2.1. Fabrication and evaluation of CMDs enantiomers.

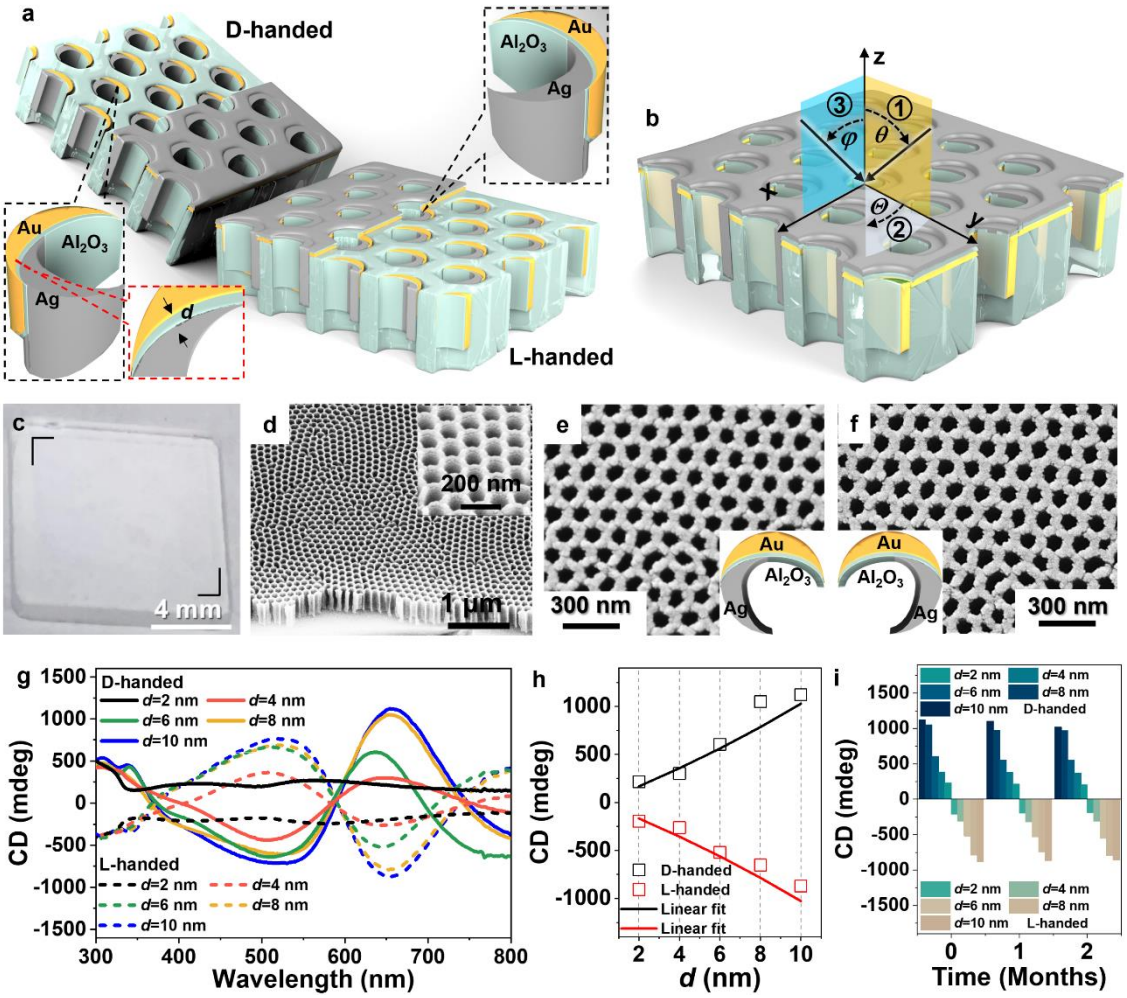

Figure 1. Fabrication and evaluation of the CMDs enantiomers. (a) Schematic representation of the D- and L-handed CMDs enantiomers. (b) Illustration of the reference coordinate system of the CMDs and the deposition orientation of Au, Ag and Al_2O_3 films on the UAAO template. Photograph (c) and SEM image (d) of the UAAO template. SEM images of the D- (e) and L-handed (f) CMDs enantiomers. (g) CD spectra of the CMDs enantiomers with the Al_2O_3 film thickness of *d*=2 nm, 4 nm, 6 nm, 8 nm and 10 nm, respectively. (h) Relationship between the CD intensities and *d* at the wavelength of 661 nm. (i) Time-stability of the chiroptical response of the CMDs enantiomers with different Al_2O_3 film thickness examined at the wavelength of 661 nm.

The D- and L-handed CMDs enantiomers, as illustrated in Figure 1(a), were fabricated using a two-step glancing angle deposition (GLAD) process on the ultrathin anodic aluminum oxide (UAAO) templates. In Figure 1(b), the CMDs was placed in the cartesian coordinate system to visually depict the preparation process. An Au film with the thickness of 20 nm was deposited on the UAAO at an angle of θ=45° in the *y*-*z* plane. Subsequently, an Al_2O_3 film was deposited onto the surface of the Au film using atomic layer deposition (ALD) at an ambient temperature of 150°. Next, the UAAO template was rotated at an angel of Θ=+90°, and then an Ag film with a thickness of 20 nm was deposited on the surface of the UAAO template at an angle of φ=45° in the *x*-*z* plane to complete the fabrication of the D-handed CMDs. To fabricate the L-handed CMDs, the process was identical to that of the D-handed CMDs, with the exception that the UAAO template was rotated by Θ=-90° after depositing the Au and Al_2O_3 films. The fabrication details of the CMDs enantiomers were illustrated in Supplementary Note 1.

The UAAO template with a silica substrate, as shown in Figure 1(c), was chosen to prepare the CMDs enantiomers and subsequently perform transmission CD measurement. Figure 1(d) is the scanning electron microscopy (SEM) image of the UAAO with a thickness of 400 nm, the diameter and the sidewall thickness of the nanohole are 100 nm and 25 nm, respectively. Figures 1(e) and 1(f) are SEM images of the D- and L-handed CMDs enantiomers with *d*=10 nm, respectively, revealing that the chiral nanostructures have been uniformly prepared on the UAAO templates. The chiral nanostructures, prepared with centimeter-scale dimensions (1 cm×1 cm), enable the chiroptical response of the CMDs enantiomers to be evaluated using a commercial CD spectrometer (Chirascan) with a beam size of 8 mm. This utilization of the CD spectrometer ensures the acquisition of reliable examination results. The chiroptical response of the CMDs enantiomers was adjusted by controlling the thickness of the Al_2O_3 films. Figure 1(g) is the CD spectra of the D- and L-handed CMDs with the Al_2O_3 thickness of *d*=2 nm, 4 nm, 6 nm, 8 nm and 10 nm, respectively, revealing that the chiroptical response of the CMDs can be enhanced by increasing the thickness of the Al_2O_3 films. In addition, the CD spectra of the D- and L-handed CMDs exhibit a bisignate feature, revealing mirror symmetry between these CMDs enantiomers. This characteristic is consistent across different thicknesses of the Al_2O_3 films, as shown in Figure 1(g). The dissymmetry factors (*g*-factors) of the CMDs with different Al_2O_3 film thicknesses have been experimentally measured, as shown in Supplementary Figure S2. The *g*-factor of CMDs enantiomers with *d*=10 nm reached 0.1 at the wavelength of 661 nm, indicating excellent chiroptical responses of the CMDs enantiomers. Figure 1(h) is the *d*-dependence of the chiroptical response of the CMDs at the wavelength of 661 nm, and the relationship between the CD intensity and *d* has formation as

I_{CD}=±[62.5+107.5d], revealing that the chiroptical response of the CMDs enantiomers can be experimentally customized based on the thickness of the Al_2O_3 films. In addition, the *d*-dependence of the CD intensity of the other two CMDs samples was examined at the wavelength of 661 nm, and the repeatability examination result of the chiroptical response of the two CMDs is shown in Supplementary Figure S3.

Furthermore, considering that the Ag material is used in the preparation process of the CMDs enantiomers, the CD spectra of the CMDs enantiomers with different storage times were examined to assess the time stability of the chiroptical response of the CMDs enantiomers. Taking the wavelength of 661 nm as an example, Figure 1(i) shows the corresponding CD intensity of the CMDs at one-month interval. The time stability of the CMDs enantiomers examined by CD spectra can be seen in Supplementary Figure S4. It is worth noting that the relative standard deviation (RSD) of the time stability for the chiroptical response of the D-handed CMDs with different film thicknesses is 5.89% (*d*=2 nm), 2.00% (*d*=4 nm), 5.75% (*d*=6 nm), 4.64% (*d*=8 nm) and 5.11% (*d*=10 nm), suggesting that the chiroptical response of the CMDs remains remarkably stable when stored in ambient environments for a period of two months. This high-level stability ensures the successful execution of subsequent experiments relying on the CMDs enantiomers.

The influence of the Al_2O_3 film thickness on the chiroptical response of the CMDs enantiomers has been further investigated. We have quantified the Al_2O_3 film thickness by combining the scanning transmission electron microscopy (STEM) and the energy-dispersive spectroscopy (EDS). Ultrathin slices of the D- and L-handed CMDs were extracted from the regions between the black and red dashed lines in Figures 2(a_1) and (a_2), respectively. The orientation of the STEM imaging direction for the ultrathin slices of the D- and L-handed CMDs are indicated by the red arrows in the insets of Figure 2(a_1) and 2(a_2), respectively. The location of the Al_2O_3 film can be confirmed according to the EDS image, and the contrast of different components in the STEM image can confirm the Al_2O_3 film thickness. STEM images of the D- and L-handed CMDs with measured thicknesses of *d*=2 nm, 6 nm, and 10 nm are shown in Figures 2(b_1, b_2), (d_1, d_2) and (f_1, f_2), respectively, indicating that ALD deposition accurately controls the thickness of the Al_2O_3 film to adjust the chiroptical response of the CMDs enantiomers. The corresponding EDS imaging for the D- and L-handed CMDs with *d*=2 nm, 6 nm, and 10 nm, are shown in Figures 2(c_1, c_2), (e_1, e_2) and (g_1, g_2), respectively. In addition, the D- and L-handed CMDs enantiomers with *d*=4 nm and 8 nm have also been verified by STEM and EDS, shown in Supplementary Figure S5.

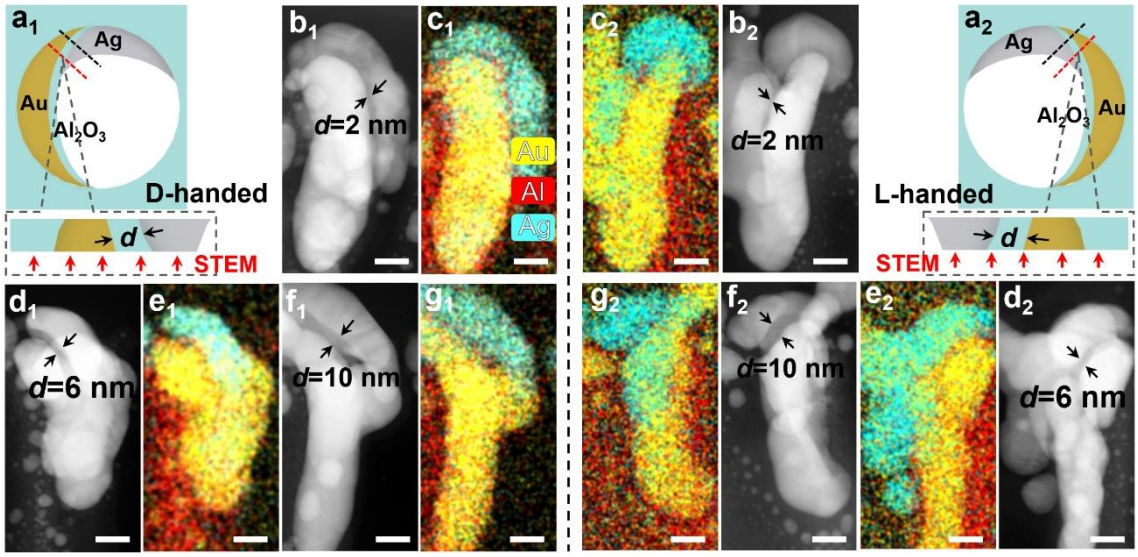

Figure 2. Examination of Al_2O_3 film thickness of CMDs enantiomers. Taking samples to test the Al_2O_3 film thickness for D- (a_1) and L-handed (a_2) CMDs enantiomers. Insets in (a_1) and (a_2) are the samples obtained from the areas between the black and red dashed lines in (a_1) and (a_2), respectively, and the red arrows indicates the STEM imaging direction for the samples. STEM images of the D- and L-handed CMDs with Al_2O_3 film thickness of *d*=2 nm (b_1, b_2), 6 nm (d_1, d_2), and 10 nm (f_1, f_2), respectively. EDS images for D- and L-handed CMDs with *d*=2 nm (c_1, c_2), 6 nm (e_1, e_2), and 10 nm (g_1, g_2), respectively. Scale bars: 20 nm.

The *d*-dependence of the chiroptical response of the D- and L-handed CMDs enantiomers was calculated by the finite difference time domain (FDTD) method. The structural model used in the simulation is shown in Supplementary Figure S6. Figure 3(a) gives the calculated CD spectra of the CMDs enantiomers with *d*=2 nm, 4 nm, 6 nm, 8 nm and 10 nm, respectively [Calculated details see Method 3]. Note that, *d* mainly affects the CD intensity, although it also has a minor effect on the chirality resonant wavelength. The *g*-factors of the CMDs with different Al_2O_3 film thicknesses have been theoretically calculated, as shown in Supplementary Figure S7. The *g*-factor of the CMDs enantiomers with *d*=10 nm reached 0.3 at the wavelength of 661 nm, indicating outstanding chiroptical responses of the CMDs enantiomers. Figure 3(b) is the *d*-dependence of the chiroptical response of the CMDs at the wavelength of 661 nm, and the relationship between the CD intensity and *d* has formation as $I_{CD}=\pm[1041.9+508.9d]$, revealing that the chiroptical response of the CMDs also can be theoretically customized according to the thickness of the Al_2O_3 film. The calculation results qualitatively reproduce the experimental data at the wavelength of 661 nm. The disparity in the CD intensity between the experimental and calculated spectra can be attributed primarily to the surface scattering loss caused by the surface roughness of the prepared CMDs.[18]

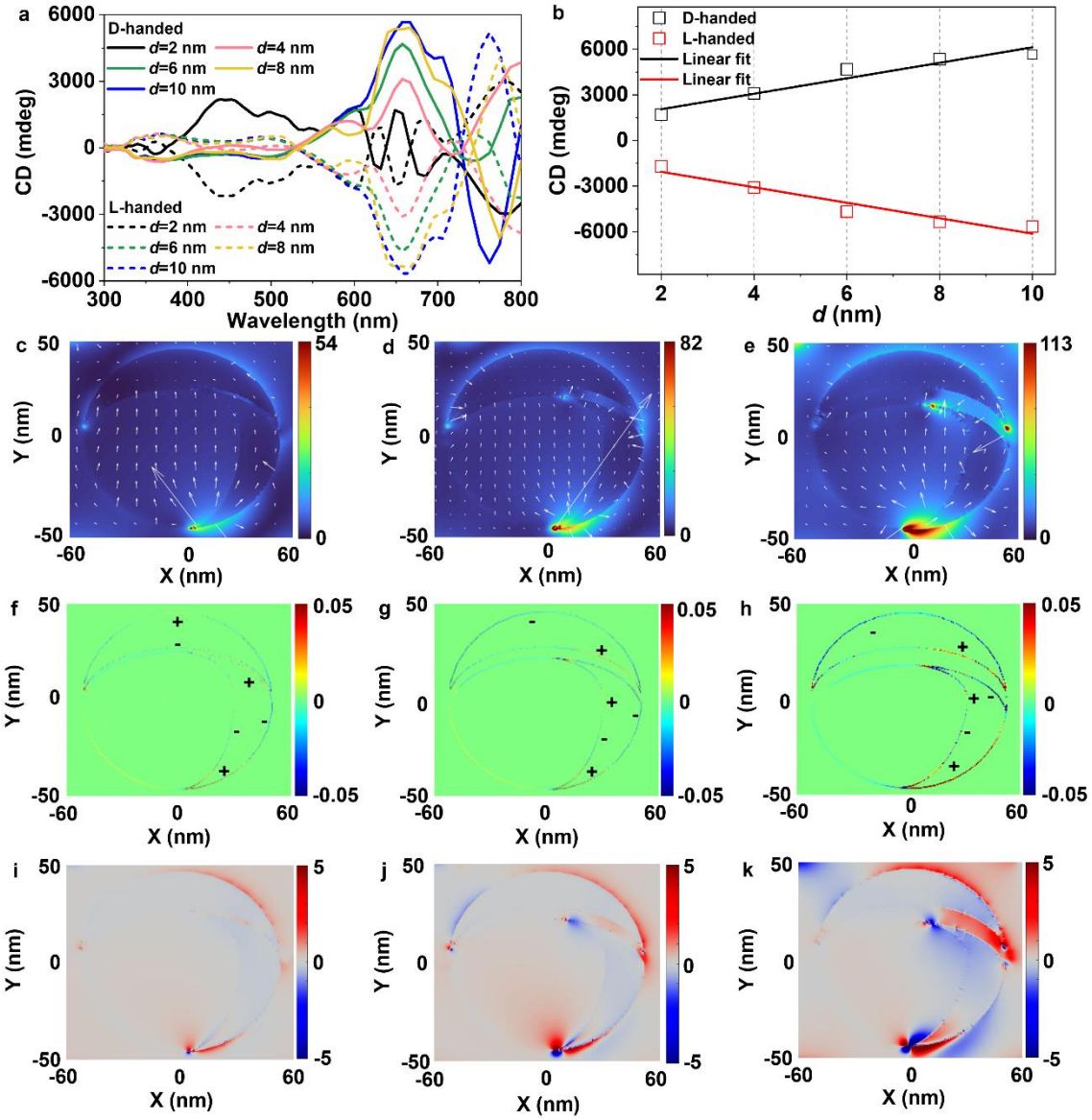

Figure 3. Theoretical calculations on CMDs enantiomers. (a) Theoretically predicted CD spectra of the D- and L-handed CMDs with *d*=2 nm, 4 nm, 6 nm, 8 nm and 10 nm. (b) Relationship between CD intensities and *d*. Electric-field distributions $|E/E_0|$ of the D-handed CMDs with *d*=2 nm (c), *d*=6 nm (d), and *d*=10 nm (e) under the illumination of RCP at the wavelength of 661 nm. Charge distribution of the D-handed CMDs with *d*=2 nm (f), *d*=6 nm (g), and *d*=10 nm (h) under the illumination of RCP at the wavelength of 661 nm. Superchiral field $|C/C_0|$ distribution of the D-handed CMDs with *d*=2 nm (c), *d*=6 nm (d), and *d*=10 nm (e) under the illumination of RCP at the wavelength of 661 nm, with C and C_0 being of optical chirality of the CMDs and the circularly polarized light (CPL) in free space, respectively.

In order to explore the enhancement mechanism of the chiroptical response of the CMDs with different Al_2O_3 thicknesses, the electric-field, charge and superchiral-field distributions of the CMDs enantiomers with different Al_2O_3 thicknesses were calculated based on FDTD

method.[19] In the case of right-handed circular polarization (RCP) illumination, the calculation result of the electric-field distributions of the D-handed CMDs with *d*=2 nm, 6 nm, and 10 nm at the wavelength of 661 nm are shown in Figure 3 (c-e), respectively. The electric-field distributions of the D-handed CMDs with *d*=4 nm and 8 nm are shown in Supplementary Figure S8. Note that, the electric-field distributions and intensities of the D-handed CMDs are strongly influenced by *d*, the electric-field enhancement factor ($EF=|E/E_0|$) and the hot-spot numbers increase as *d* increase, with E and E_0 being of the amplitudes of the electric field of the CMDs and the incident electric field,[20] respectively. In addition, in the case of L-handed CMDs irradiated by RCP, the EF decreases as *d* increases, as shown in Supplementary Figure S9. In a word, as *d* increase, the gradually increasing difference in the plasmon-enhanced electric field and distribution between D- and L-handed CMDs indicates the gradually enhanced chiroptical response. This can be attributed to the gradual increase of *d* enhancing the asymmetry of the CMDs,[21] which leads to the asymmetric excitation current oscillation, so as to provide a strong local surface plasmonic resonance at the tip apex of the structural unit, thereby inducing a gradual enhancement of the electric-field intensity. Furthermore, to evaluate the effect of the nanogap on the chiroptical response of the CMDs, the CMDs without nanogap were prepared by the preparation process shown in Supplementary Figure S1, in addition to removing the Al_2O_3 film. The measured CD spectrum and STEM image of the CMDs without Al_2O_3 film is shown in Supplementary Figure S10, there is no obvious CD resonance peak near the wavelength of 500 nm, revealing that the contribution of the Al_2O_3 film to the CD spectrum of the CMDs.

In order to reveal the electric-field enhancement mechanism of the CMDs by Al_2O_3 layer, the calculated charge distributions for the CMDs with *d*=2 nm, 6 nm, and 10 nm are shown in Figures 3(f-h), respectively, in the case of RCP illumination. The calculated charge distributions for the CMDs with *d*=4 nm and 8 nm are shown in Supplementary Figure S11. The upper crescent layers of the CMDs exhibit dipole resonance characteristics, and the resonance direction changes as *d* increases.[22] The lower crescent layer exhibits quadrupole resonance under conditions of *d*=2 nm, 4 nm, 6 nm, and 8 nm, except for dipole and quadrupole mixed resonance in the case of *d*=10 nm.[22] At *d*=2 nm, 4 nm, 6 nm, and 8 nm, the dipole resonance mode of the upper crescent layer interacts with the quadrupole resonance mode of the lower crescent layer to induce a hybrid mode, causing the electric field to be confined to the tip of the lower crescent layer, and the electric field intensity increases with the increase of *d*, as shown in Figures 3(c-e). At *d*=10 nm, the dipole resonance mode of the upper crescent layer interacts with the dipole and quadrupole mixed resonance mode of the lower crescent layer to generate

another hybridized mode, resulting in an electric field confined on the nanogaps and the tip of the lower crescent layer, simultaneously.

The chiroptical response of the CMDs with different *d* are calculated, and the near-field chirality distributions of the D-handed CMDs with *d*=2 nm, 6 nm, and 10 nm are shown in Figure 3(i-k), and the near-field chirality distributions of the D-handed CMDs with *d*=4 nm and 8 nm are shown in Supplementary Figure S12. The near-field chirality intensity of D-handed CMDs increases as *d* increases, and the chirality intensity is mainly distributed in the nanogap and the tip apex of the crescent layer, consistent with the variation of the electric field intensity. The enhancement mechanism of the nanogap induced chiroptical response is as follows: The introduction of the nanogap with gradually increasing thicknesses enhance the asymmetry of the chirality nanostructures, thereby improving the chiroptical response of the CMDs.[21] The combination of the crescent layers and the nanogap generate more plasmonic hot-spots with significantly enhanced chiroptical response. In addition, the interaction of the dipole-quadrupole and the dipole-dipole resonances induce the chiroptical response enhancement.[23] However, the chiroptical response of the CMDs cannot be infinitely enhanced by increasing *d*, and the CD intensity of the CMDs with *d*=12 nm is smaller than that of the CMDs with *d*=10 nm. The main reason for this phenomenon may be that the further increase of *d* reduces the effective coupling of the electromagnetic modes between the upper and lower lunar layers, and the calculation and experimental results see Supplementary Figure S13. Therefore, *d*=10 nm is the optimal parameter for CMDs to have the strongest chiroptical response.

2.2. CMDs enantiomers on flexible substrate.

By combining the UAAO template and the GLAD process, the CMDs enantiomers on the flexible substrate can be realized. As illustrated in Figure 4(a), the UAAO template was transferred from the silica substrate to the scotch tape, which offers exceptional flexibility and bending capacity, along with high transmissivity in the visible band. Consequently, the UAAO template, after being transferred onto the scotch tape, as shown in Figure 4(b), can be furtherly used to fabricate the CMDs with excellent mechanical bending capacity. As sketched in Figure 4(c), the chiral nanostructure was deposited on the UAAO template by using the GLAD process shown in Fig. 1(b).

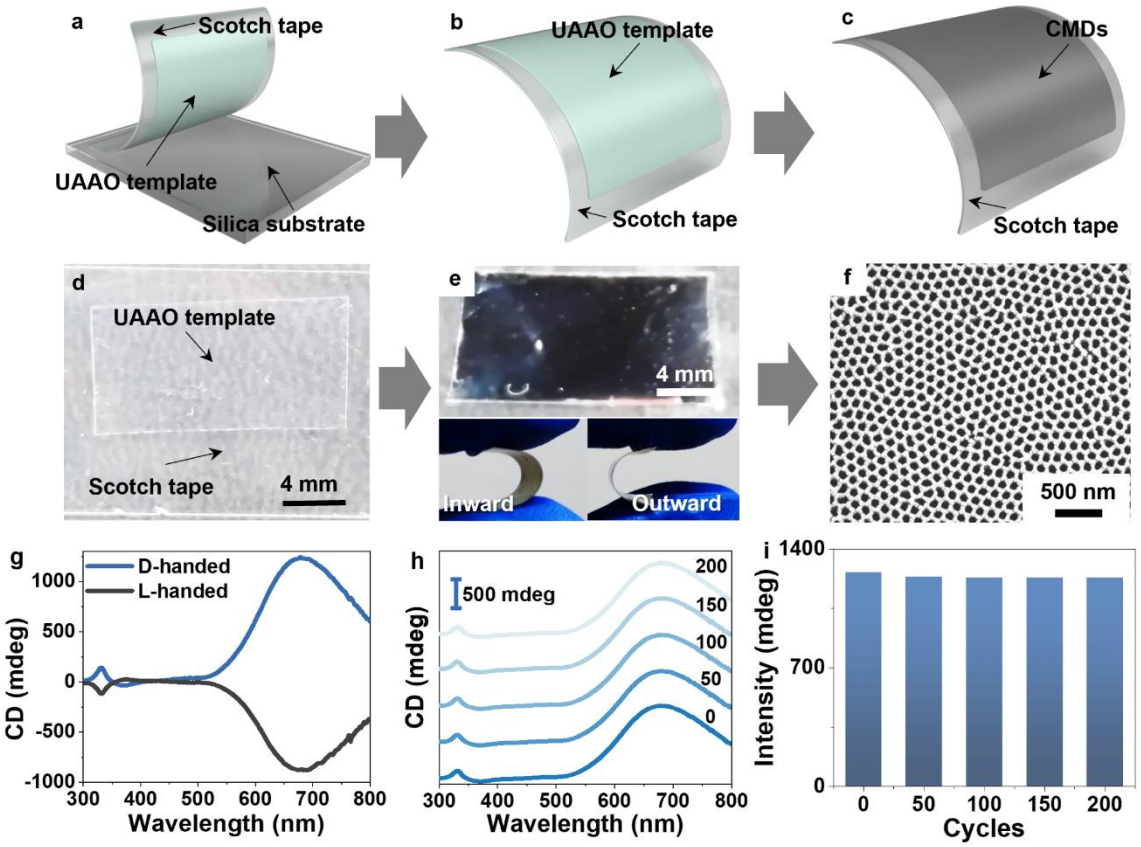

Figure 4. Preparation of CMDs enantiomers on flexible substrate. Sketch map of the UAAO template transferred from the silica substrate (a) to the scotch tape (b). (c) CMDs enantiomers on the scotch tape. Photographs of the UAAO template on the scotch tape (d) and the D-handed CMDs with *d*=10 nm on scotch tape (e). (f) SEM image of the D-handed CMDs in (e). (g) CD spectra of the D- and L-handed CMDs with *d*=10 nm on the scotch tapes. (h) CD spectra of the D-handed CMDs after undergoing different numbers of bending cycles, with an inward - outward bend being defined as a cycle. (i) Histogram of CD intensity at the wavelength of 680 nm after undergoing different numbers of bending cycles.

The photograph of the UAAO template on the scotch tape demonstrates the successful transfer of the 20 mm×10 mm UAAO template onto the scotch tape with exceptional flatness, ensuring a smooth and even surface. Figure 4(e) is the photograph of the D-handed CMDs on the scotch tape, in which the D-handed CMD consists of Au, Al_2O_3, and Ag films with thicknesses of 20 nm, 10 nm and 20 nm, respectively. In addition, to prevent thermal deformation of the scotch tape, the chamber temperature was set to be 80° during the deposition process of Al_2O_3 film by ALD. Figure 4(f) is the SEM image of D-handed CMDs after undergoing inward and outward bending. Note that, the mechanical deformation induced by bending does not compromise the integrity of the chiral nanostructure on the UAAO template. The chiroptical response of D- and L-handed CMDs on scotch tape was obtained using a

commercial CD spectrometer (Chirascan), which is represented by the blue and black curves in Figure 4(g), respectively. The CD spectra of the D- and L-handed CMDs exhibit a bisignate feature, indicating the mirror symmetry between these CMDs enantiomers on a flexible substrate. However, compared to the CD spectra in Figure 1 (g), the CD spectra in Figure 4 (g) do not show a significant CD peak at the wavelength of 500 nm. The reason is that after transferring the AAO template to the scotch tape, the ALD ambient temperature is set to 80° to prevent contamination of the ALD chamber. However, lower temperatures limit the growth rate of Al_2O_3 layer and reduce the deposition film quality, resulting in uneven deposition of the Al_2O_3 film.[24] This can be observed from the CD spectra of the CMDs without Al_2O_3 film, as shown in Supplementary Figure S10. When there is no Al_2O_3 film as the spacer layer, the CD peak near 500 nm disappeared, and only the main peak near 660 nm was preserved. Figure 4(h) shows the CD spectra of the D-handed CMDs after undergoing different times of bending cycles. As can be seen, bending cycles does not affect the chirality intensity of the CMDs. Figure 4(i) shows the histogram of the CD intensities at the wavelength of 680 nm obtained from Figure 4(h), the RSD of the CD intensities with different bending times is 1.13%, revealing that the chiroptical response of the CMDs maintains excellent consistency after the disappearance of the mechanical bending.

2.3. Active tunability of chirality sign and intensity of CMDs.

The chiroptical response of the CMDs can be actively tuned by bending the flexible substrate to different curvature radii. As shown in Figure 5(a), to realize bending of the CMDs with a specific curvature radius *R*, the two ends of the flexible substrate are fixed onto a glass slide. The curvature radius can be adjusted by moving one end of the flexible substrate via a displacement table. Figure 5(b) give the photographs of the D-handed CMDs on the flexible substrate with bending radii of *R*=10 mm, 7.8 mm, 4.2 mm, 3.2 mm, 2.5 mm, 2.1 mm, 1.8 mm, 1.5 mm and 1.3 mm, respectively. The corresponding *R*-dependence of chiroptical response of the D- and L-handed CMDs is shown in Figure 5(c). The CD spectra of the D- and L-handed CMDs consistently maintain an excellent bisignate feature, confirming the mirror symmetry between these CMDs enantiomers on the flexible substrate with varying bending radii. The black square symbols shown in Figure 5(d) represent the *R*-dependence of the CD intensity of the D-handed CMDs at the wavelength of 441 nm, and the black curve represents the fitting result that correlates the CD intensity with the bending radius *R*, as the following formation

$$I_{CD} = 153 - \frac{1343}{\sqrt{2\pi} \times 0.59R} \exp\left\{-\left[\ln\left(\frac{R}{3.4}\right)\right]^{2.8}\right\} \quad (1)$$

Note that, the chirality sign of the D-handed CMDs can be switched by controlling the bending radii of the flexible substrate. The critical bending radius for chiral sign switching is *R*=5 mm based on the fitting result. As an example, the D-handed CMDs with CD intensity of 230 mdeg can be switched to the L-handed CMDs with CD intensity of -210 mdeg, with bending radius *R*=10 mm decreasing of *R*=2.1 mm. Figure 5(e) is the histogram of the chirality sign switching by bending the flexible substrate from *R*=10 mm to 2.1 mm with three cycles, demonstrating excellent repeatability of chiral sign switching through bending the flexible CMDs. The CD spectrum of the chirality sign switching of the D-handed CMDs see Supplementary Figure S14.

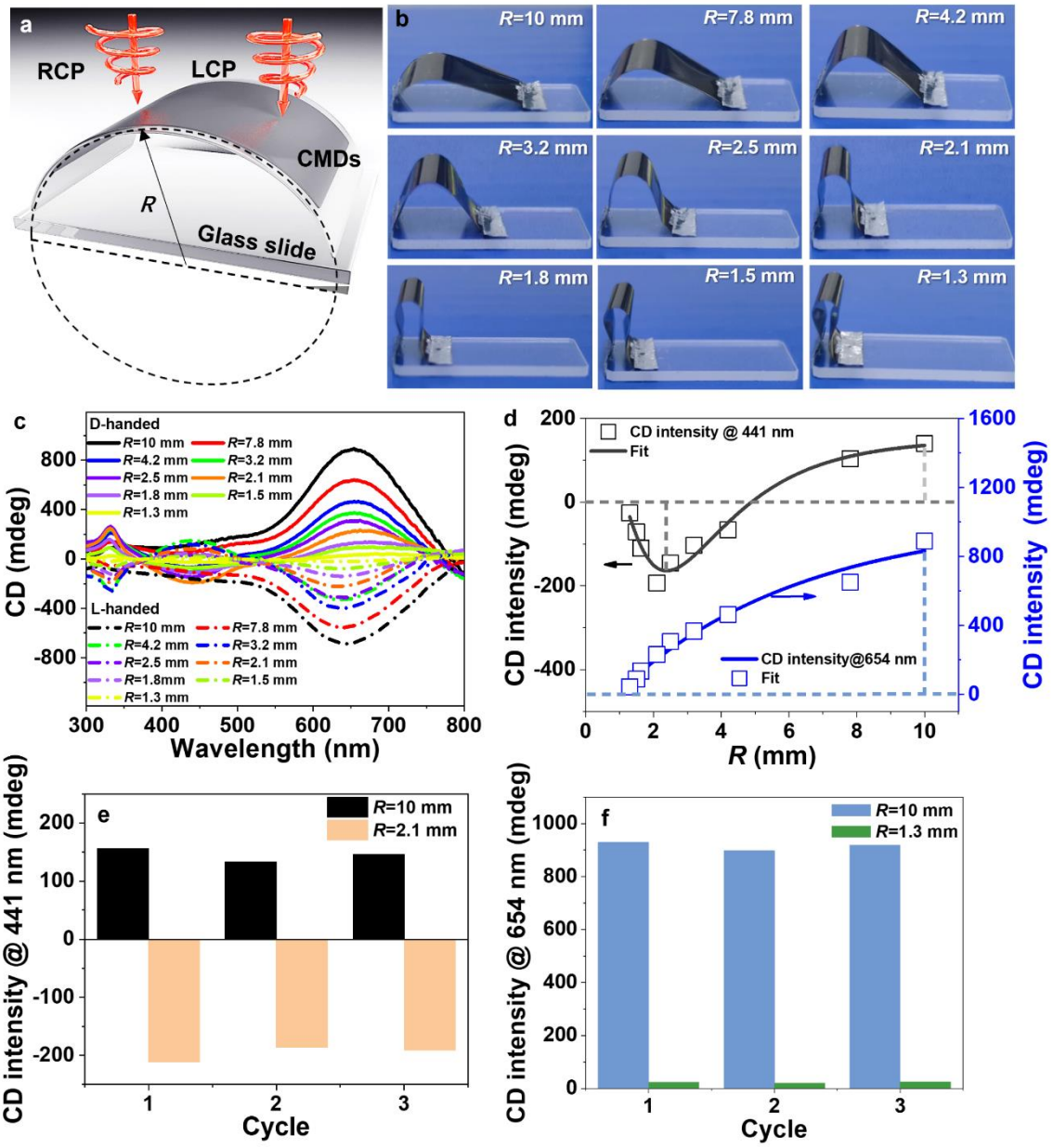

Figure 5. Active tunability of chiroptical response of CMDs. (a) Sketch map of CMDs fixed on a glass slide with a bending radius of *R*. (b) Photographs of D-handed CMDs fixed on the glass slide with *R*=10 mm, 7.8 mm, 4.2 mm, 3.2 mm, 2.5 mm, 2.1 mm, 1.8 mm, 1.5 mm, and

1.3 mm, respectively. (c) Measured CD spectra of D- and L-handed CMDs with different banding radii in (b). (d) *R*-dependence of the measured CD intensity of the D-handed CMDs at the wavelength of 441 nm (black square symbols) and 654 nm (blue square symbols). Black and blue curves are the fitting result for the measured CD intensity at the wavelength of 441 nm and 654 nm, respectively. (e) Chirality sign switching at the wavelength of 441 nm by bending the D-handed CMDs from *R*=10 mm to 2.1 mm with three cycles. (f) Chirality intensity turning on-off at the wavelength of 654 nm by bending the D-handed CMDs from *R*=10 mm to *R*=1.3 mm.

The blue square symbols shown in Figure 5(d) represent the *R*-dependence of the CD intensity of the D-handed CMDs at the wavelength of 654 nm, and the blue curve represents the fitting result, which correlates the CD intensity with the bending radius *R* with formation as

$$I_{CD} = 1026 \exp\left(\frac{R}{0.55}\right) - 1203 \tag{2}$$

note that, as the bending radius of the flexible substrate decreases, the CD intensity exhibits a monotonic exponential attenuation trend. By decreasing the bending radius from 10 mm to 1.3 mm, the CD intensity of the D-handed CMD at the wavelength of 654 nm can be adjusted from 900 mdeg to 30 mdeg. This observation reveals that the chiroptical response of the D-handed CMDs can be controlled effectively, allowing it to be turned on and off by adjusting the bending radius of the flexible substrate. Figure 5(f) is the histogram of the chirality intensity turning on-off by bending the flexible substrate from *R*=10 mm to 1.3 mm with three cycles, demonstrating excellent repeatability of the chiral intensity turning on-off through bending the flexible CMDs. The CD spectrum of turning on-off the chiroptical response of the D-handed CMDs see Supplementary Figure S15.

To clarify the causes for the stressmechanically reconfigurable chiroptical response of the flexible CMDs, we performed the numerical simulation by the FDTD method. Figures 6(a_1-a_4) are four spatial orientations between a D-handed CMDs unit and the illumination light source with the included angle of 0°, 30°, 60° and 75°, respectively. Since there is only one chiral structural unit, the influence of the spatial orientation of the structural unit on the chiroptical response can be obtained. Figure 6(b) is the corresponding simulation result of the CD spectra in the case of the four included angles. The histograms in Figure 6(c) and (d) show the angle-dependence characteristic of the D-handed CMDs unit at the wavelength of 476 nm and 693 nm, respectively. Note that, as the included angle increases, the CMDs unit exhibits the chirality sign switching and the chirality intensity turning on-off functions at the wavelength of 476 nm

and 693 nm, respectively, basically coinciding with the examination result of the chirality sign switching and the chirality intensity turning on-off of the flexible CMDs shown in Figure 5(d).

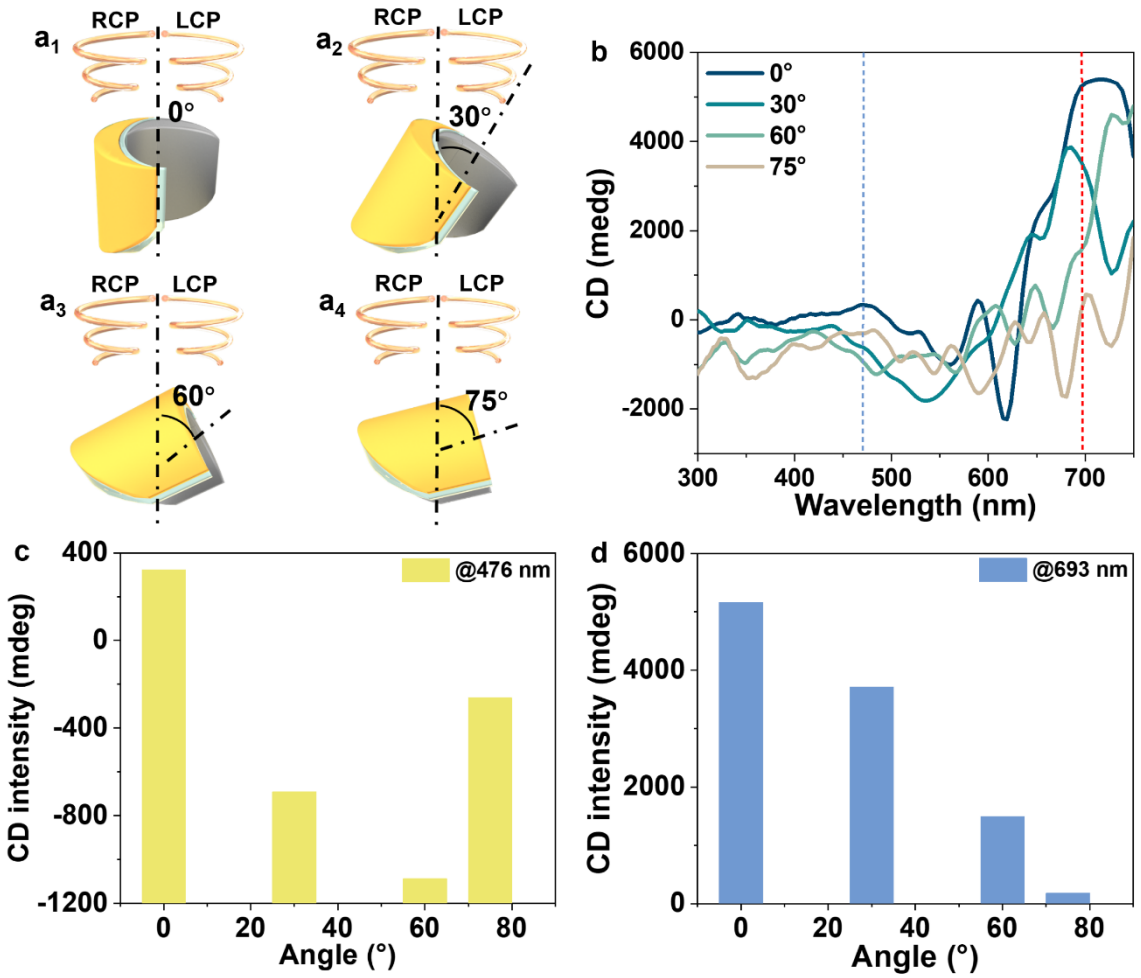

Figure 6. Simulation of the chiroptical response of the D-handed CMDs with different spatial orientations. Spatial configuration between the D-handed CMDs unit and the illumination light sources with an included angle of 0° (a_1), 30° (a_2), 60°(a_3) and 75° (a_4). (b) Simulated CD spectra of the D-handed CMDs unit with four different included angles in (a_1-a_4). Angle-dependence of the CD intensity of the D-handed CMDs at the wavelength of 476 nm (c) and 693 nm (d).

3. Conclusion

In summary, we have presented a low-cost and convenient procedure to realize large-area stressmechanically reconfigurable CMDs enantiomers in the visible band. Our approach allows for the dynamic tunability of optical chirality by employing a flexible substrate. The CMDs enantiomers with centimeter scale were prepared by a two-step GLAD process on the UAAO templates supported by a silica substrate. The CD measurement result proves that the CMDs exhibit a maximum dissymmetry factor of 0.1 at the wavelength of 661 nm. Furthermore, by transferring the CMDs from the silica substrate to a flexible film, we have demonstrated

chirality sign switching and the chirality intensity turning on-off by bending the flexible CMDs to the desired curvature radius. This work provides an effective strategy for fabricating centimeter-scale visible-band CMDs enantiomers with dynamically tunable chiroptical response. It opens up new possibilities for activity-tunable CMDs enantiomers, and offers promising prospects for developing novel nanophotonic platforms for advancing chiral optical sensing.

4. Experimental Methods

Materials: The UAAO templates used in this experiment were purchased from Shenzhen Topo Fine Film Technology Co. The silver (99.9%) and gold (99.999%) particles for thermal evaporation deposition were purchased from ZhongNuo Advanced Material （Beijing） Technology Co., Ltd.

Instrumentation: The surface topography of the CMDs enantiomers was imaged by SEM (FEI Verios-G4) under an accelerating voltage of 15 kV. Ultrathin samples of the CMDs enantiomers were performed by a ultrathin slicer (LEICA-UC7FC7) working at room temperature, and then imaged by high-resolution Transmission Electron Microscopy (TEM, FEI Talos F200X TEM） with an accelerating voltage of 200 KV and an electron gun with Schottky thermal field emission. The CD spectra of CMDs were measured by a commercial circular dichroism spectrometer (Chirascan, Photophysics Ltd.) with a scan step of 2 nm.

Numerical simulations: The chiroptical response of CMDs enantiomers was simulated by the FDTD method (Lumerical). By referring to the measured structural parameters of CMDs, the structure models of the D- and L-handed enantiomers were built and then imported into FDTD to calculate the chiroptical response of the CMDs enantiomers within the window of 300 nm~800 nm. A chirality unit with one nanohole surrounded by four-quarter nanoholes was used to simulate an infinite period nanohole array under two-dimensional periodic boundary conditions. To obtain more accurate calculation results, the mesh grid size was set to 1 nm for the planarization of the nanostructure. Circularly polarized light (CPL) source was simulated by two separate plane wave sources that are orthogonal in position and differ in polarization phase by -90° and +90°. The optical parameters of Au and Ag material were adapted from Johnson and Christy with material fitting adjustments,[25] and the optical parameters of Al_2O_3 were adapted from the Palik handbook.[26] The CD spectrum of the CMDs is calculated by[27]

$$\mathrm{CD}\left(\mathrm{mdeg}\right)=\Delta\mathrm{A}\times\frac{\ln 10}{4}\times\frac{180}{\pi}\times 1000 \tag{3}$$

where, $\Delta A=A_{LCP}-A_{RCP}$ is the differential absorption spectra of CMDs, with A being converted by the transmission spectrum

$$A = \lg\left(\frac{1}{T}\right) \quad (4)$$

with T being of the transmission spectra calculated based on the Beer-Lambert law. Transmission spectra of the CMDs for d=2 nm, 4 nm, 6 nm, 8nm and 10 nm under RCP and illumination are shown in Figure S16.

Supporting Information

Supporting Information is available from the Wiley Online Library or from the author.

Acknowledgements

This work was supported by National Natural Science Foundation of China (NSFC) (11974282, 91950207, 12374358, 12174310). Doctoral Dissertation Innovation Fund of Northwestern Polytechnical University (CX2021039).

Conflict of Interest

The authors declare no conflict of interest.

Data Availability Statement

The data that support the findings of this study are available from the corresponding author upon reasonable request.

Received: ((will be filled in by the editorial staff))

Revised: ((will be filled in by the editorial staff))

Published online: ((will be filled in by the editorial staff))

References

[1] a) M. Zhang, G. Qing, T. Sun, *Chem. Soc. Rev.* **2012**, 41, 1972; b) G. Palermo, G. Lio, M. Esposito, L. Ricciardi, M. Manoccio, V. Tasco, A. Passaseo, A. Luca, G. Strangi, *ACS Appl. Mater. Inter.* **2020**, 12, 30181; c) L. Warning, A. Miandashti, L. McCarthy, Q. Zhang, C. Landes, S. Link, *ACS Nano* **2021**, 15, 15538.

[2] a) W. Zhang, B. Ai, P. Gu, Y. Guan, Z. Wang, Z. Xiao, G. Zhang, *ACS Nano* **2021**, 15, 17657; b) Z. Liu, J. Ai, P. Kumar, E. You, X. Zhou, X. Liu, Z. Tian, P. Bouř, Y. Duan, L. Han, N. Kotov, S. Ding, S. Che, *Angew. Chem. Int. Ed.* **2020**, 59, 15226; c) Y. Ma, Z. Cao, J. Hao, J. Zhou, Z. Yang, Y. Yang, J. Wei, *J. Phys. Chem. C* **2020**, 124, 24306; d) C. Wang, C. Hao, W. Ma, A. Qu, C. Chen, J. Xu, C. Xu, H. Kuang, L. Xu, *Adv. Mater.* **2021**, 33, 2102337.

A. B. Author 1, C. D. Author 2, *Adv. Mater.* **2020**, *18*, 2001086; b) A. Author 1, B. Author 2, *Adv. Funct. Mater.* **2019**, *16*, 1900965.

[3] a) C. Chen, L. Gao, W. Gao, C. Ge, X. Du, Z. Li, Y. Yang, G. Niu, J. Tang, *Nat. Commun.* **2019**, 10, 1927; b) H. Kim, R. Kim, S. Namgung, N. Cho, J. Son, K. Bang, M. Choi, S. Kim,

K. Nam, J. Lee, J. Oh, *Adv. Sci.* **2022**, 9, 2104598; c) W. Li, Z. Coppens, L. Besteiro, W. Wang, A. Govorov, J. Valentine, *Nat. Commun.* **2015**, 6, 8379.

[4] a) L. Kang, S. Rodrigues, M. Taghinejad, S. Lan, K. Lee, Y. Liu, D. Werner, A. Urbas, W. Cai, *Nano Lett.* **2017**, 17, 7102; b) L. Kang, C. Wang, X. Guo, X. Ni, Z. Liu, D. Werner, *Nano Lett.* **2020**, 20, 2047; c) E. Plum, N. Zheludev, *App. Phy. Lett.* **2015**, 106, 221901; d) Y. Huang, T. Xiao, Z. Xie, J. Zheng, Y. Su, W. Chen, K. Liu, M. Tang, J. Zhu, P. Müller-Buschbaum, L. Li, *ACS Appl. Mater. Inter.* **2021**, 13, 45890.

[5] a) Y. Chen, J. Gao, X. Yang, *Laser Photonics Rev.* **2018**, 12, 1800198.; b) J. Gansel, M. Thiel, M. Rill, M. Decker, K. Bade, V. Saile, G. Freymann, S. Linden, M. Wegener, *Science* **2009**, 325, 1513.

[6] a) X. Yin, M. Schäferling, A. Michel, A. Tittl, M. Wuttig, T. Taubner, H. Giessen, *Nano Lett.* **2015**, 15, 4255; b) L. Zhang, K. Gao, F. Lu, L. Xu, M. Rahmani, L. Sun, F. Gao, W. Zhang, T. Mei, *Nano Lett.* **2022**, 22, 7628; c) Q. Wang, E. Rogers, B. Gholipour, C. Wang, G. Yuan, J. Teng, N. Zheludev, *Nat. Photonics* **2016**, 10, 60; d) O. Abdelraouf, Z. Wang, H. Liu, Z. Dong, Q. Wang, M. Ye, X. Wang, Q. Wang, H. Liu, *ACS Nano* **2022**, 16, 13339; e) P. Moitra, Y. Wang, X. Liang, L. Lu, A. Poh, T. Mass, R. Simpson, A. Kuznetsov, R Paniagua-Dominguez, *Adv. Mater.* **2023**, 35, 2205367; f) L. Lu, Z. Dong, F. Tijiptoharsono, R. Ng, H. Wang, S. Rezaei, Y. Wang, H. Leong, P. Lim, J. Yang, R. Simpson *ACS Nano* **2021**, 15, 19722.

[7] Z. Wu, X. Chen, M. Wang, J. Dong, Y. Zheng, *ACS Nano* **2018**, 12, 5030.

[8] K. Morisawa, T. Ishida, T. Tatsuma, *ACS Nano* **2020**, 14, 3603.

[9] P. Probst, M. Mayer, V. Gupta, A. Steiner, Z. Zhou, G. Auernhammer, T. König, A. Fery, *Nat. Mater.* **2021**, 20, 1024.

[10] T. Driscoll, H. Kim, B. Chae, B. Kim, Y. Lee, N. Jkerst, S. Palit, D. Smith, M. Ventra, D. Basov, *Science* **2009**, 325, 1518.

[11] M. Suda, Y. Thathong, V. Promarak, H. Kojima, M. Nakamura, T. Shiraogawa, M. Ehara, H. Yamamoto, *Nat. Commun.* **2019**, 10, 2455.

[12] T. Kan, A. Isozaki, N. Kanda, N. Nemoto, K. Konishi, H. Takahashi, M. Kuwata-Gonokami, K. Matsumoto, I. Shimoyama, *Nat. Commun.* **2015**, 6, 8422.

[13] A. Kuzyk, M. Urban, A. Idili, F. Ricci, N. Liu, *Sci. Adv.* **2017**, 3, e1602803.

[14] S. Chen, Z. Liu, H. Du, C. Tang, C. Ji, B. Quan, R. Pan, L. Yang, X. Li, C. Gu, X. Zhang, Y. Yao, J. Li, N. Fang, J. Li, *Nat. Commun.* **2021**, 12, 1299.

[15] R. Malatong, T. Sato, J. Kumsampao, T. Minato, M. Suda, V. Promarak, H. Yamamoto, *Small* **2023**, 2302714.

[16] B. Feringa, R. van Delden, N. Koumura, E. Geertsema, *Chem. Rev.* **2000**, 100, 1789.

[17] R. Fan, Y. Zhou, X. Ren, R. W. Peng, S. C. Jiang, D. H. Xu, X. Xiong, X. Huang, R. M. Wang, *Adv. Mater.* **2015**, 27, 1201.

[18] a) Z. Y. Wang, B. Ai, Z. W. Zhou, Y. D. Guan, H. Möhwald, G.Zhang, *ACS Nano* **2018**, 12, 10914; b) Y. D. Guan, Z. Y. Wang, B. Ai, C. Chen, W. Zhang, Y. Wang, G.Zhang, *ACS Appl. Mater. Interfaces* **2020**, 12, 50192.

[19] M. Cen, J. Wang, J. Liu, H. L. He, K. Li, W. F. Cai, T. Cao, Y. J. Liu, *Adv. Mater.* **2022**, 34, 2203956.

[20] K. Du, P. Li, H. Wang, K. Gao, R. B. Liu, F. Lu, W. Zhang, T. Mei, *Adv. Opt. Mater.* **2021**, 9, 2001771.

[21] X. Duan, Y. Song, N. Liu, *Nanoscale* **2015**, 7, 17237.

[22] F. Zhou, Z. Li, Y. N. Xia, *J. Phys. Chem. C* **2008**, 112, 20233.

[23] E. Hendry, T. Carpy, J. Johnston, M. Popland, R. V. Mikhaylovskiy, A. J. Lapthorn, S. M. Kelly, L. D. Barron, N. Gadegaard, M. Kadodwala, *Nat. Nanotechnol.* **2010**, 5, 783.

[24] a) S. E. Potts, W. M. M. Kessels, *Coordin. Chem. Rev.* **2013**, 23, 3254; b) R. Bryan, *J. Appl. Crystallogr.* **1997**, 30, 419.

[25] P. Johnson, R. Christy, *Phys. Rev. B* **1972**, 6, 4370.

[26] E. D. Palik, *Handbook of Optical Constants of Solids* **1985**, 1, 429.

[27] G. D. Fasman, *Circular Dichroism and the Conformational Analysis of Biomolecules.* Springer, New York, **1996**.

In order to achieve continuous and reversible adjustment of the chiroptical response of Chiroptical meta-devices (CMDs), we designed and prepared visible-band, large-area flexible CMDs, and achieved chiral sign switching and chiral intensity turn on-off by bending the flexible CMDs to the desired curvature radius.

Lu Zhang, Jie Wang, Lei Xu, Feng Gao, Wending Zhang*, and Ting Mei*

Stressmechanically Reconfigurable Chiroptical Meta-devices in Visible-Band

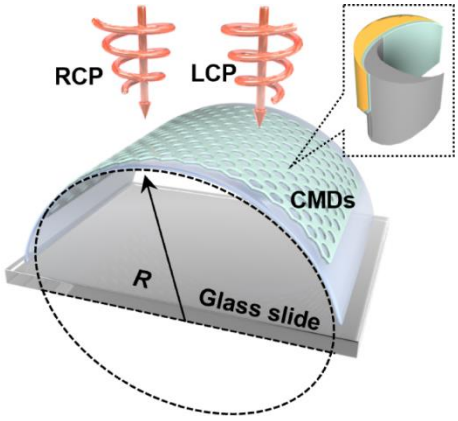

Supporting Information

Stressmechanically Reconfigurable Chiroptical Meta-devices in Visible-Band

Lu Zhang, Jie Wang, Lei Xu, Feng Gao, Wending Zhang, and Ting Mei**

Supplementary Note 1: Fabrication process of CMDs enantiomers

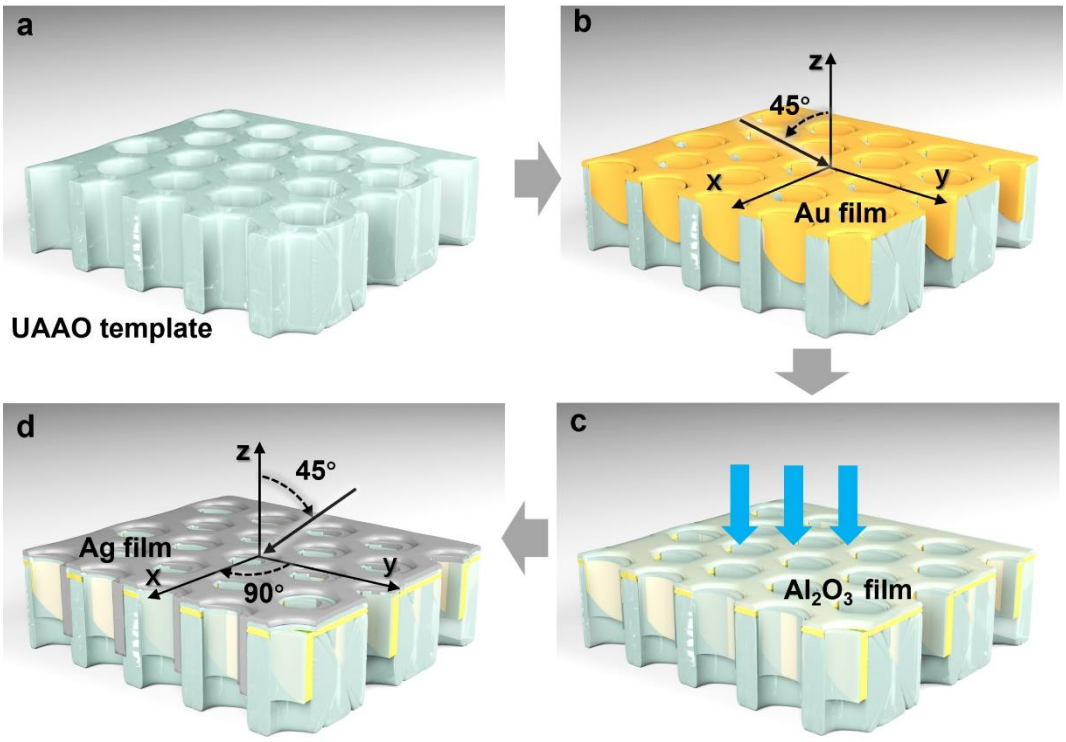

Supplementary Figure S1: Fabrication process of D- and L-handed CMDs enantiomers.

The schematic diagram of the preparation process of enantiomeric CMDs is shown in Figure S1. First, the UAAO template, as shown in Figure S1 (a), was fixed on the sample holder at a tilt angle of 45° for thermal evaporative coating. A 20 nm thick Au film was deposited on the UAAO template, as shown in Figure S1 (b). Next, the Al_2O_3 film was deposited on the surface of Au film by ALD at ambient temperature of 150°, as shown in Figure S1 (c). Finally, as shown in Figure S1 (d), the UAAO template was fixed on the sample holder at an angle of 45° and then the UAAO template was rotated by an azimuth angle of 90° clockwise or counterclockwise to deposit a 20 nm Ag film, to obtain the D- and L-handed CMDs enantiomers, respectively.

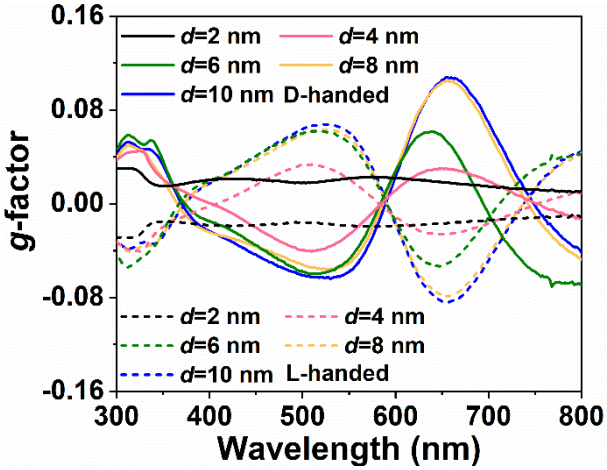

Supplementary Figure S2: Experimentally measured *g*-factors of the CMDs enantiomers with the Al_2O_3 film thickness of *d*=2 nm, 4 nm, 6 nm, 8 nm and 10 nm, respectively.

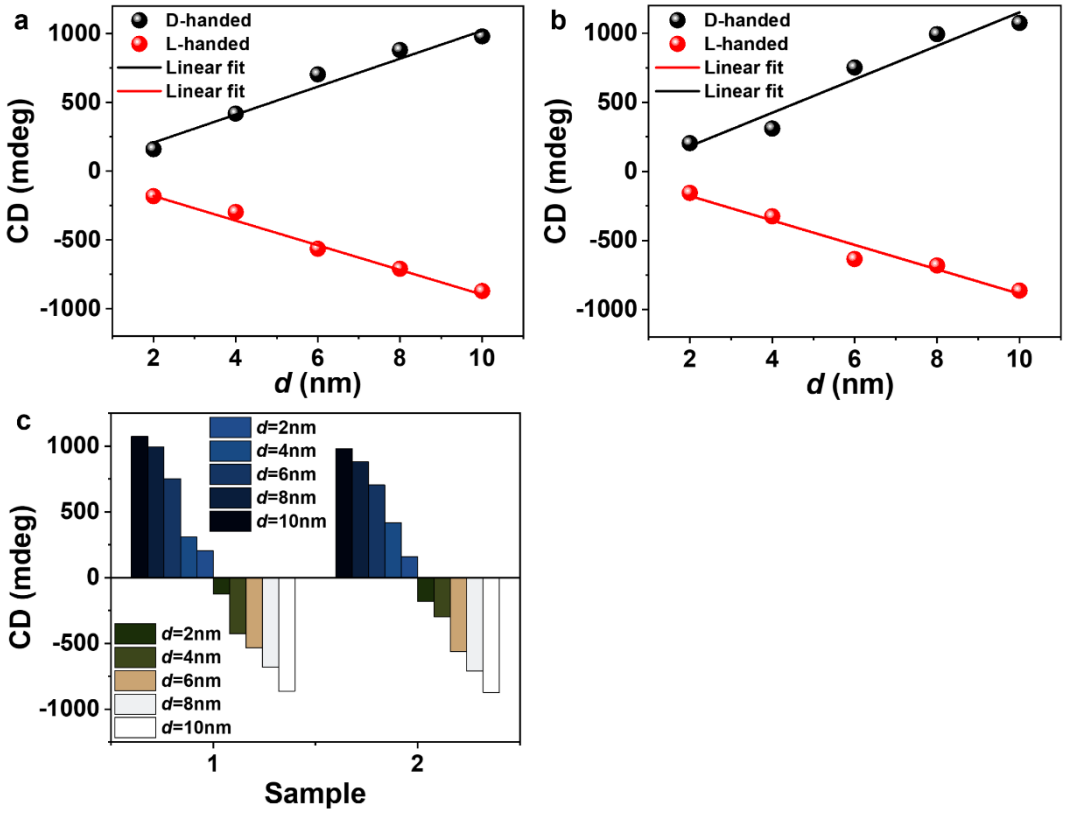

Supplementary Figure S3: *d*-dependence of the CD intensity of the sample 1 (a) and sample 2 (b) at the wavelength of 661 nm, respectively. (c) Repeatability examination of the CD intensity of two CMDs sample at the wavelength of 661 nm.

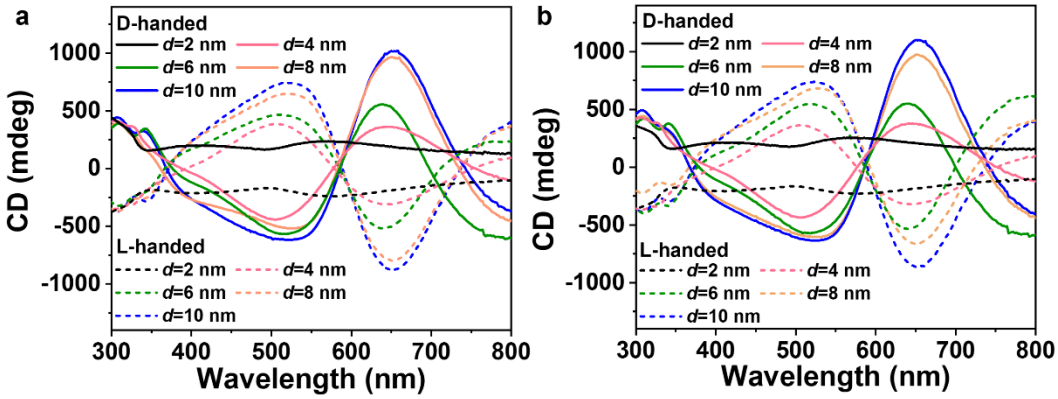

Supplementary Figure S4: CD spectra of D- and L-handed CMDs with *d*=2 nm, 4 nm, 6 nm, 8 nm and 10 nm placed in ambient environmental for two (a) and three months (b), respectively.

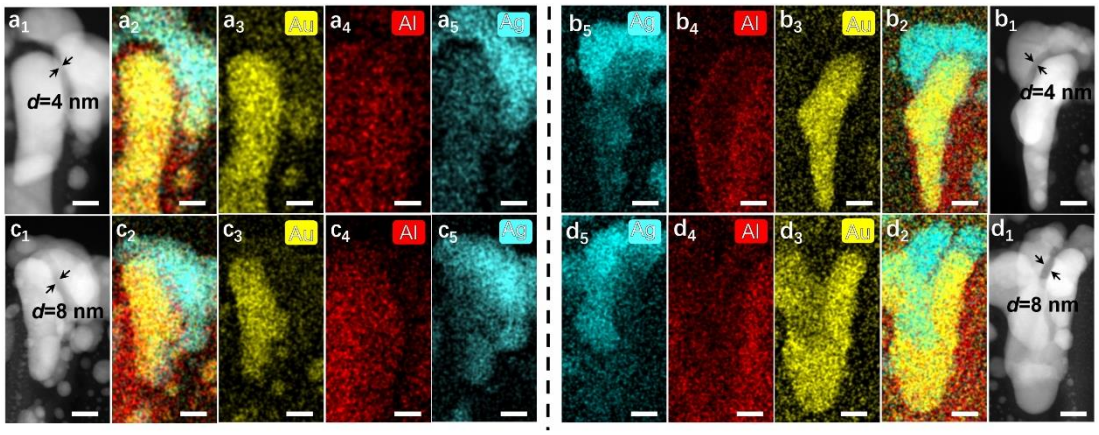

Supplementary Figure S5: STEM images of the D- and L-handed CMDs with Al_2O_3 thicknesses of *d*=4 nm (a_1, b_1) and 8 nm (c_1, d_1), respectively. EDS images for D-and L- CMDs with *d*=4 nm (a_2-a_5, b_2-b_5) and 8 nm (c_2-c_5, d_2-d_5), respectively. Scale bars: 20 nm.

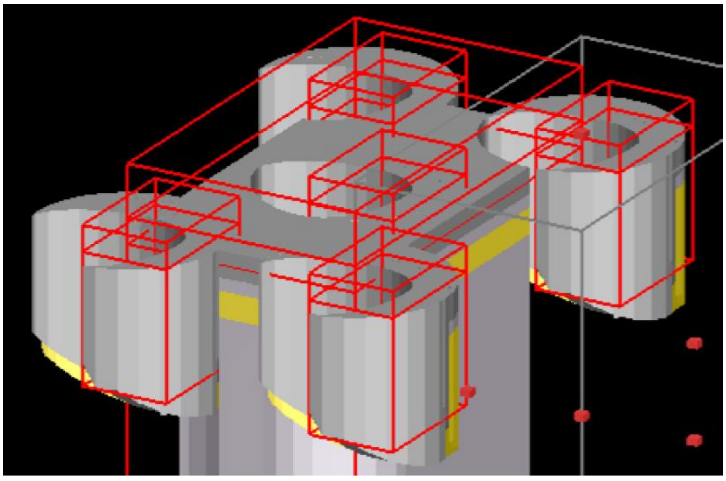

Supplementary Figure S6: Simulation model of D-handed CMDs for FDTD calculation.

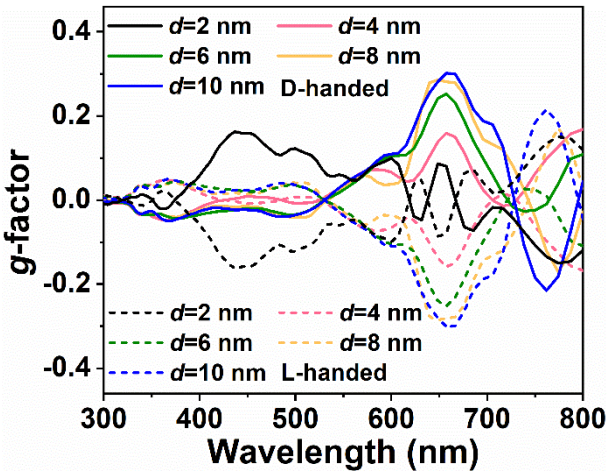

Supplementary Figure S7: Theoretically simulated *g*-factors of CMDs enantiomers with the Al_2O_3 film thickness of *d*=2 nm, 4 nm, 6 nm, 8 nm and 10 nm, respectively.

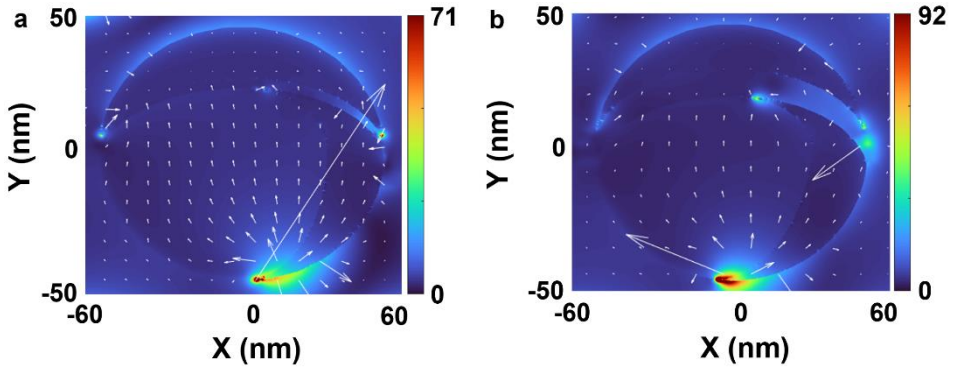

Supplementary Figure S8：Electric field distributions $|E/E_0|$ of the D-handed CMDs with *d*=4 nm (a), and *d*=8 nm (b) under the illumination of RCP at the wavelength of 661 nm.

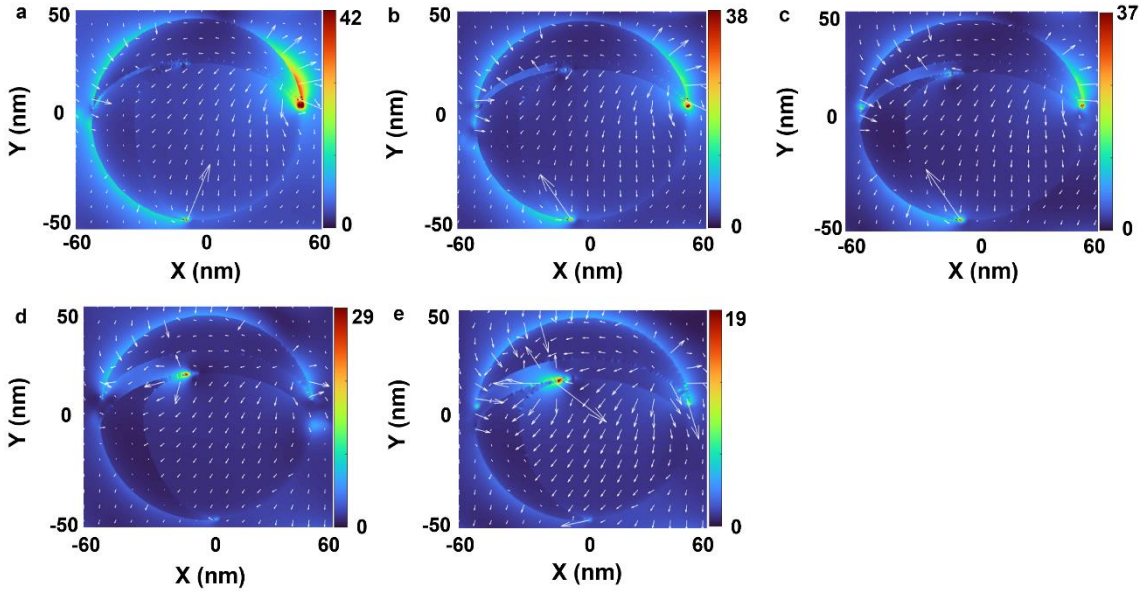

Supplementary Figure S9：Electric field distributions $|E/E_0|$ of the L-handed CMDs with *d*=2 nm (a), *d*=4 nm (b), *d*=6 nm (c), *d*=8 nm (d), and *d*=10 nm (e) under the illumination of RCP at the wavelength of 661 nm.

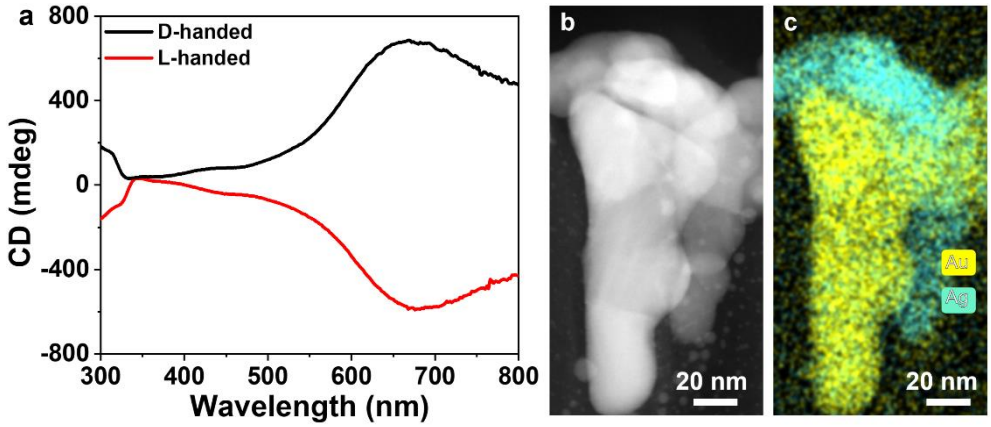

Supplementary Figure S10：(a) CD spectra of the D- and L-handed CMDs without Al_2O_3 film. STEM (b) and EDS (c) images of the D-handed CMDs without Al_2O_3 film.

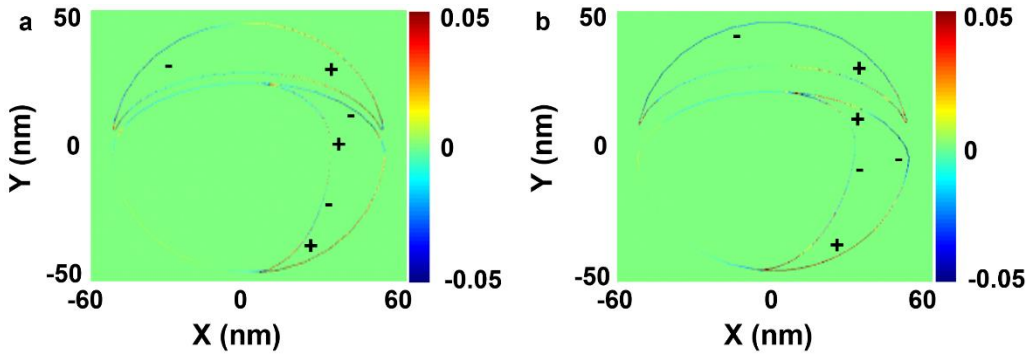

Supplementary Figure S11：Charge distribution of the D-handed CMDs with *d*=4 nm (a), and *d*=8 nm (b) under the illumination of RCP at the wavelength of 661 nm.

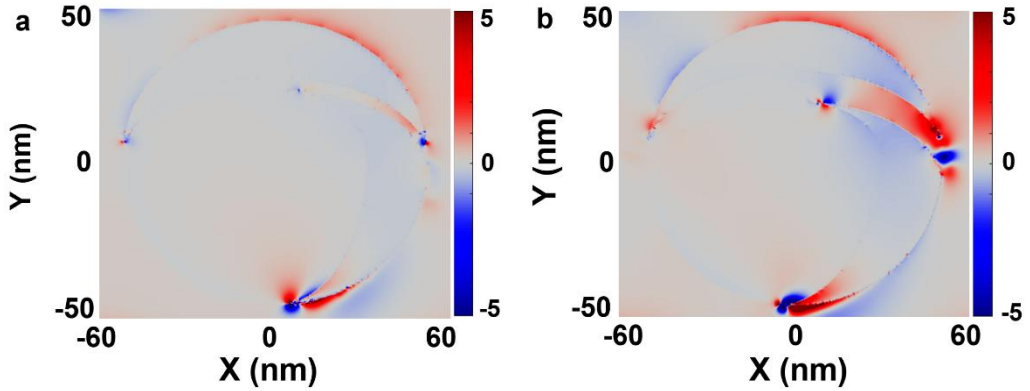

Supplementary Figure S12 : Superchiral field distributions $|C/C_0|$ of the D-handed CMDs with *d*=2 nm (c), *d*=6 nm (d), and *d*=10 nm (e) under the illumination of RCP at the wavelength of 661 nm.

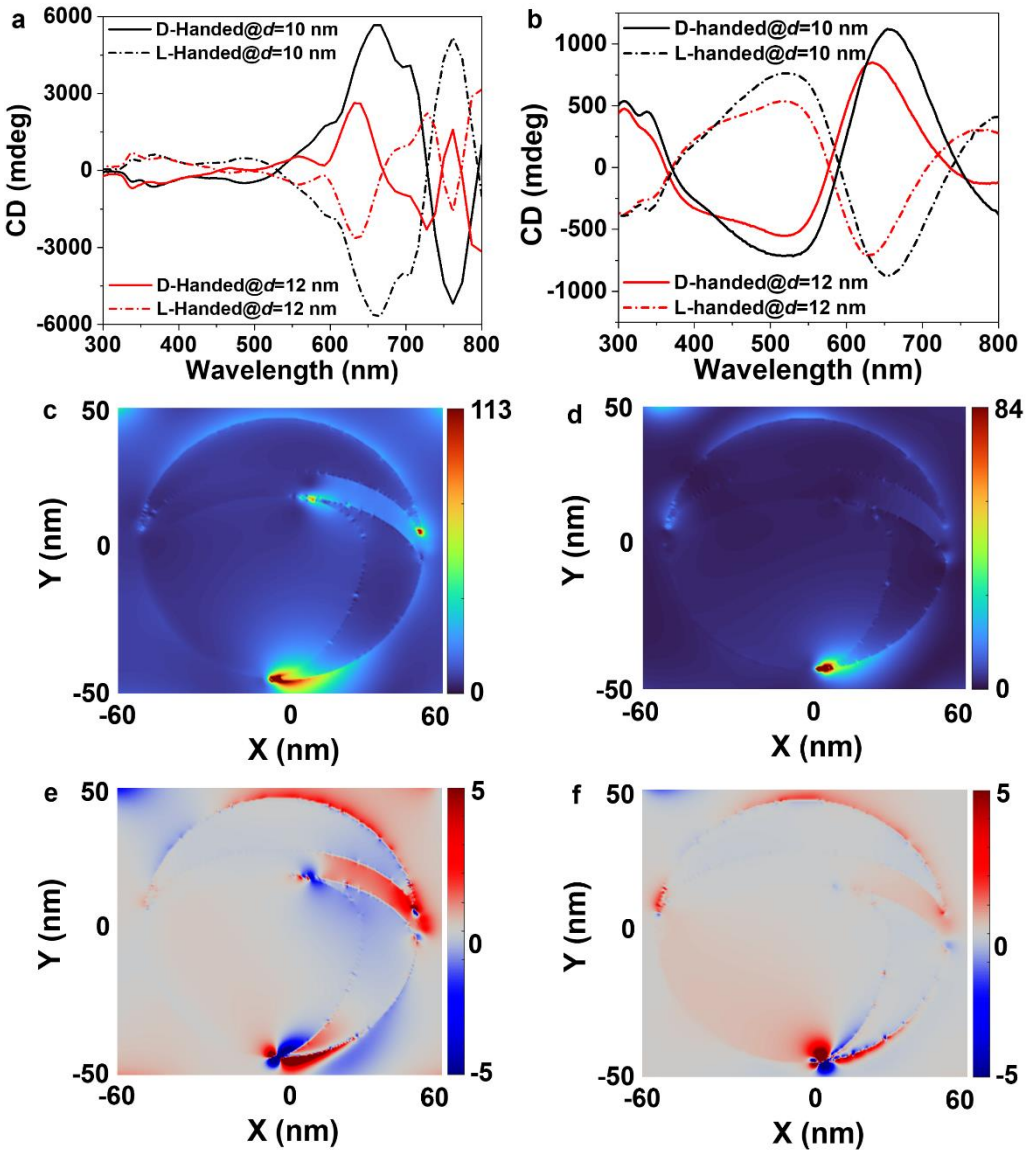

Supplementary Figure S13 : Simulated (a) and measured (b) CD spectra of the D- and L-handed CMDs with *d*=10 nm and 12 nm. Electric field distributions $|E/E_0|$ of the D-handed CMDs with *d*=10 nm (c) and *d*=12 nm (d) under the illumination of RCP at the wavelength of 661 nm. Superchiral field distributions $|C/C_0|$ of the D-handed CMDs with *d*=10 nm (e) and *d*=12 nm (f) under the illumination of RCP at the wavelength of 661 nm.

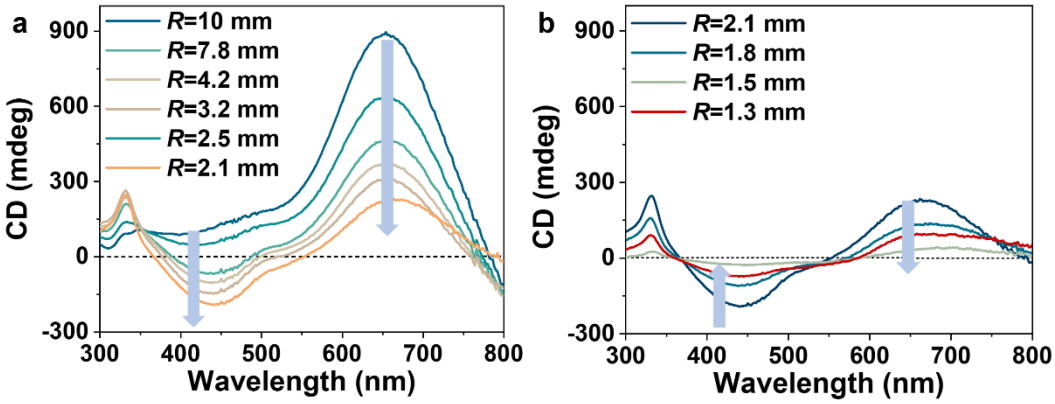

Supplementary Figure S14：CD spectra of the D-handed CMDs with curvature radius *R*=10 mm, 7.8 mm, 4.2 mm, 3.2 mm, 2.5 mm, and 2.1 mm (a) and *R*=2.1 mm, 1.8 mm, 1.5 mm and 1.3 mm (b), respectively.

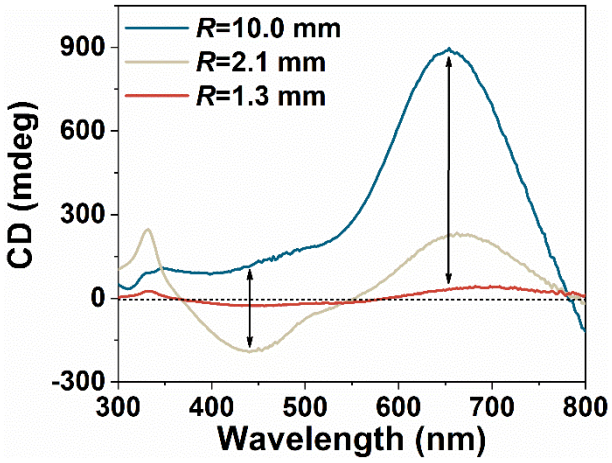

Supplementary Figure S15：CD spectra of the D-handed CMDs with curvature radius of *R*=10 mm, 2.1 mm and 1.3 mm, respectively.

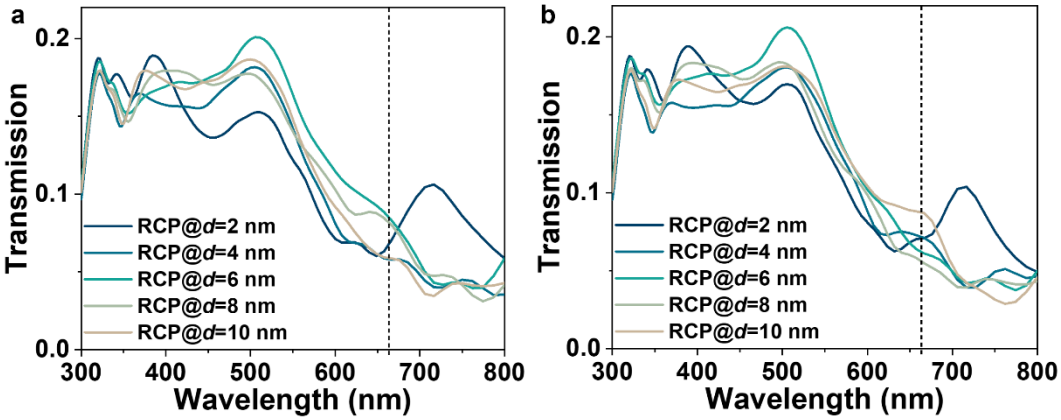

Supplementary Figure S16: Transmission spectra of the D-handed CMDs for *d*=2 nm, 4 nm, 6 nm, 8 nm, and 10 nm under RCP (a) and LCP (b) illuminations.